Syngas Conversion Hot Paper

International Edition: DOI: 10.1002/anie.201705714
German Edition: DOI: 10.1002/ange.201705714

Intermediate Product Regulation in Tandem Solid Catalysts with Multimodal Porosity for High-Yield Synthetic Fuel Production

*Nicolas Duyckaerts, Mathias Bartsch, Ioan-Teodor Trotuş, Norbert Pfänder, Axel Lorke, Ferdi Schüth, and Gonzalo Prieto**

Abstract: *Tandem catalysis is an attractive strategy to intensify chemical technologies. However, simultaneous control over the individual and concerted catalyst performances poses a challenge. We demonstrate that enhanced pore transport within a Co/Al_2O_3 Fischer–Tropsch (FT) catalyst with hierarchical porosity enables its tandem integration with a Pt/ZSM-5 zeolitic hydrotreating catalyst in a spatially distant fashion that allows for catalyst-specific temperature adjustment. Nevertheless, this system resembles the case of close active-site proximity by mitigating secondary reactions of primary FT α-olefin products. This approach enables the combination of in situ dewaxing with a minimum production of gaseous hydrocarbons (18 wt %) and an up to twofold higher (50 wt %) selectivity to middle distillates compared to tandem pairs based on benchmark mesoporous FT catalysts. An overall 80 % selectivity to liquid hydrocarbons from syngas is attained in one step, attesting to the potential of this strategy for increasing the carbon efficiency in intensified gas-to-liquid technologies.*

Materials with multimodal porosities that extend over several length scales hold the promise of unprecedented performance in various disciplines, from biotechnology[1] to energy storage and conversion,[2] adsorption,[3] and catalysis.[4] In catalysis, hierarchically organized porosities serve to adjust the kinetics of molecular transport, an effect that can be exploited to reduce or eliminate diffusion constraints, adjust selectivity, or extend the lifetime of solid catalysts.[5] One field in which control over molecular transport might be of particular relevance is tandem catalysis, a concept that relies on the integration of two catalysts to steer consecutive reactions in a single step. While it stands for an elegant and efficient means towards the intensification of chemical processes,[6] the integration of different solid catalysts sharing a common reaction medium often means that each catalyst operates under individually suboptimal conditions. A particularly notorious challenge is the management of the rates at which the integrated catalysts do not only individually process, but also collectively exchange molecules by transport processes to avoid, for example, derivation of intermediate products through undesired secondary reactions, something elegantly achieved in nature's enzymatic tandem reactions by complex substrate channeling phenomena.[7]

The conversion of syngas (H_2 and CO) into C_{2+} products is an area where tandem catalysis offers means to circumvent selectivity boundaries set by intrinsically unselective step growth polymerization mechanisms.[8] In this context, the tandem integration of highly active cobalt-based Fischer–Tropsch synthesis (FTS) and zeolite-based hydrocracking catalysts to produce liquid hydrocarbons from syngas in a single step has been proposed as an attractive approach towards the simplification, miniaturization, and intensification of syngas-to-liquid technologies.[8c–e] This is required for the valorization of delocalized carbon resources, such as lignocellulosic biomass or stranded natural gas, into transportable liquid hydrocarbons, circumventing the wax handling required in conventional large-scale multistep processes. However, major hurdles include the excessive production of light hydrocarbons, associated with methanation and hydrogenolysis reaction pathways on FTS catalysts operating at the higher temperatures needed for the hydrocracking reactions, alongside over-cracking of FT *n*-paraffins on the hydrocracking catalyst. These restraints limit the ultimate selectivity to the preferred middle-distillates hydrocarbon fraction (generally < 35 wt %) and undesirably contribute to the production of gaseous C_{4-} hydrocarbons (often > 30 wt %).[9]

The process showcases the potential benefits expected from an effective mitigation of undesired secondary reactions of intermediate products by adjustment of their transport rates between the active sites of the solid catalysts operating in tandem. Our recent studies with model feedstocks suggest that a higher concentration of the most primary FT products (α-olefins) on the hydrocracking catalyst could enable improved product selectivities by curbing over-cracking and limiting gas production.[10] However, the abundance of α-olefins in the hydrocarbon mixture exchanged by the integrated catalysts is generally very small as these reactive primary products are effectively depleted by pore-transport-enhanced secondary reactions, such as hydrogenation on the metal sites into *n*-paraffins, within the actual FT catalyst particles (see the Supporting Information, Figure S1).[11] Herein, we report that the design of Fischer–Tropsch catalysts with a tailored multimodal porosity provides a lever on the rates of pore molecular transport, which can be exploited to "channel" these primary FT products onto a tandem hydro-

[*] N. Duyckaerts, Dr. I.-T. Trotuş, Prof. F. Schüth, Dr. G. Prieto
Max-Planck-Institut für Kohlenforschung
Kaiser-Wilhelm-Platz 1, 45470 Mülheim an der Ruhr (Germany)
E-mail: Prieto@kofo.mpg.de
M. Bartsch, Prof. A. Lorke
Faculty of Physics and CENIDE
Universität Duisburg-Essen
Forsthausweg 2, Duisburg (Germany)
N. Pfänder
Max-Planck-Institut für Chemische Energiekonversion
Stiftstrasse 34–36, 45470 Mülheim an der Ruhr (Germany)
Supporting information and the ORCID identification number(s) for the author(s) of this article can be found under: https://doi.org/10.1002/anie.201705714.

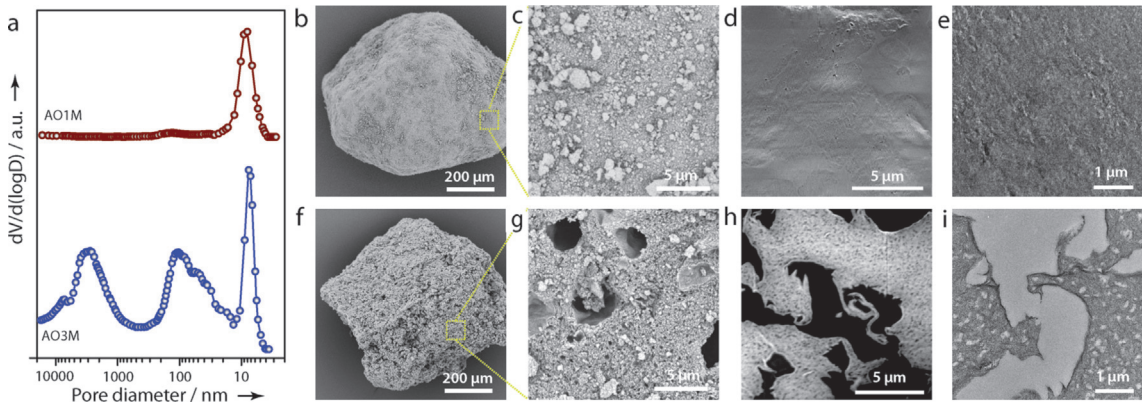

Figure 1. a) Hg intrusion pore size distributions. b, c, f, g) Representative SEM images of the microparticle outer surface. d, h) SEM cross-sectional micrographs after focused ion beam (FIB) milling. e, i) Cross-sectional bright-field TEM images of ultramicrotomed sections for unimodally mesoporous (AO1M, (b)–(e)) and trimodally meso/macro/macroporous (AO3M, (f)–(i)) γ-Al_2O_3 support materials.

cracking catalyst, enabling exceptional product patterns and efficiencies for the tandem process. To illustrate this concept, a γ-Al_2O_3 catalyst support with a singular and hierarchically organized porosity has been assembled from pseudo-boehmite nanocrystallites, using a non-ionic alkyl poly(ethylene oxide) polymer as porogen (see the Supporting Information for experimental details). Figure 1a shows the pore size distribution determined by Hg intrusion porosimetry. Compared to a commercial γ-Al_2O_3 support, for which a strictly mesoporous structure with an average pore size of 8.7 nm was determined, the soft-templated γ-Al_2O_3 displays three well-defined pore modes. Aside from a range of mesopores, with a similar average diameter of approximately 8 nm, two sets of macropores peaking in the nanometer (100 nm) and micrometer (3 µm) regimes, respectively, were identified.

Hg intrusion only reliably probes unconstrained porosity that percolates to the outer surface of the discrete microparticles (500 µm). Further insight into the spatial arrangement of the different pore systems was obtained by cross-sectional imaging at different length scales, that is, micrometer-scale SEM after focused ion beam (FIB) milling (Figure 1d, h), and nanometer-scale TEM on ultramicrotomed sections (Figure 1e, i). For the unimodally mesoporous γ-Al_2O_3, hereafter denoted as AO1M, this analysis ruled out any internal macroporosity. In the case of the soft-templated counterpart, cross-sectional imaging supplemented the Hg intrusion experiments and revealed that two sets of macropores coexist at the single-particle level that do not pertain to two populations of bimodally porous particles, which would alternatively account for the overall pore size distribution. The sets of macropores intersect mesoporous regions, which are created by the packing of γ-Al_2O_3 nanocrystals (Figure S2), leading to a truly trimodal meso/macro/macroporous architecture (AO3M).

FIB-SEM tomography was used to study the topology of the different pore systems in AO3M (Figure S3). The spatial resolution of this 3D imaging method, bridging the nanometer and micrometer regimes, renders it ideal for investigations of macroporous networks that extend over both length scales. The macropore size distributions derived by quantitative image analysis of the reconstructed tomograms were in good agreement with the Hg intrusion results (Figure S4), validating our sampling and quantification approaches and confirming the effective connection of both macropore systems to the outer surface of the microparticles. In addition, local thickness algorithms enabled the quantification of the maximum transport distance for primary FT products through the mesopore systems towards the nearest macropore network. Whereas for a strictly mesoporous material (AO1M), this maximum transport distance corresponds to the average radius of the macroscopic particles (250 µm in this case), the intersecting macropore systems in AO3M bring it down into the sub-micrometer regime. As shown in Figure 2, the histogram for the maximum 3D transport length from any point within the mesoporous network to the nanometer-sized macropore system peaks at about 100 nm. Hence, the trimodal porosity results in sub-micrometer maximum transport distances through the mesopores, which are about four orders of magnitude shorter than for a comparative mesoporous material. The combination of such a high partition of slow-transport mesoporous grains with wider pore openings in the micrometer range is only enabled by the multimodal nature of the porosity and the uniform 3D distribution of the nanometer-sized macropores.

Cobalt FTS catalysts (20 wt%) featuring ruthenium (Ru/Co atomic ratio = 0.02) as a reduction promoter[12] were synthesized on the γ-Al_2O_3 supports from nitrate precursors.[13] (S)TEM imaging revealed uniformly sized and homogeneously distributed cobalt nanoparticles confined to the mesoporous network regardless of the modality of the support porosity (Figure S5). The spatially uniform metal distribution, exclusively within the mesoporous networks, establishes a correspondence between maximum mesopore transport distances, for example, those quantified by FIB-SEM tomography for AO3M (Figure 2e), and the maximum residence time of FT products in the presence of the catalytically active cobalt nanoparticles as they diffuse from the metal sites where they are formed towards the bimodal macropore system, which is expected to represent a notably faster diffusion pathway towards the outer gas phase. Such a residence time is relevant for the probability that α-olefin primary products undergo secondary reactions, that is, re-

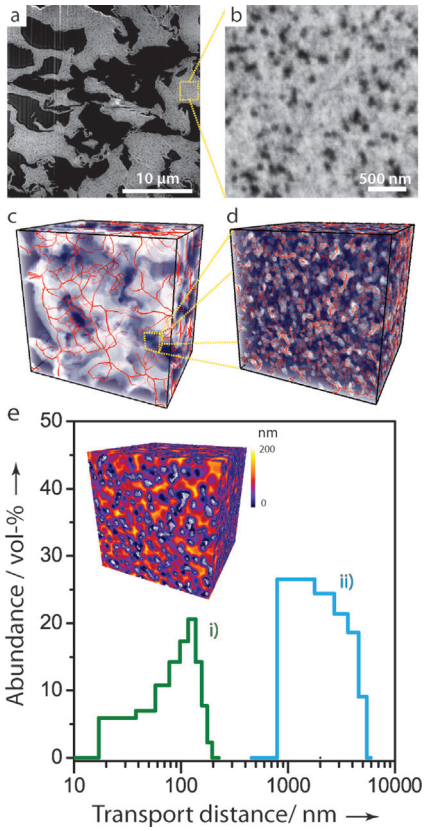

Figure 2. Cross-sectional SEM images (a, b) and reconstructed FIB-SEM tomograms (c, d) showing the micrometer- and nanometer-sized macropore systems of the trimodally porous AO3M γ-Al_2O_3. In (c) and (d), Al_2O_3 regions are depicted in blue, and red lines depict the computed macropore skeletons. e) Histograms for the maximum Euclidean distance from mesopore regions to the nanometer (i) and micrometer-sized (ii) macropore systems quantified by image analysis. The inset shows the 3D-rendered contour map for the transport distance through mesopore regions to the nanometer-sized macropore system.

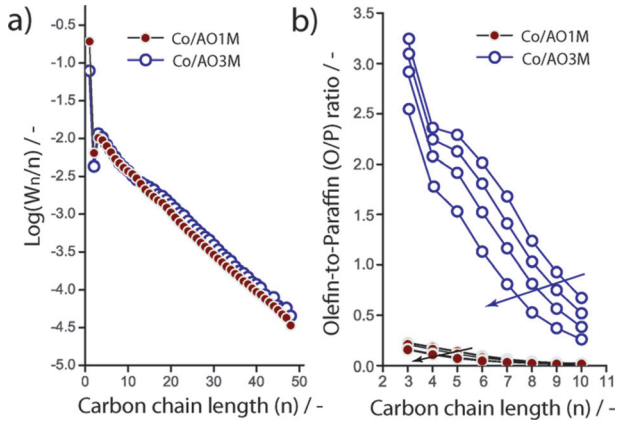

Figure 3. a) Anderson–Schulz–Flory plot of the Fischer–Tropsch hydrocarbon products and b) α-olefin-to-paraffin (O/P) molar ratio in the C_3–C_{10} chain-length range obtained with the unimodally mesoporous Co/AO1M and the trimodally meso/macro/macroporous Co/AO3M catalysts. $H_2/CO = 2$, $T = 483$ K, $P = 20$ bar. In (a), the CO conversion was $X_{CO} = 30\%$. In (b), arrows indicate increasing CO conversion levels in the range of $X_{CO} = 20$–60%.

adsorption on cobalt sites followed by chain re-insertion and/or hydrogenation into *n*-paraffin secondary products, which are known to determine the FT hydrocarbon product composition.[11b] A quantitative assessment of the pore residence times for reaction products under realistic operating conditions is very challenging, particularly for FTS catalysts, for which (partial) pore filling occurs by accumulation of long-chain hydrocarbons.[14] Fortunately, the significance of pore-transport-enhanced secondary reactions of α-olefin primary products for the ultimate hydrocarbon selectivity enabled us to use the latter as an indirect means to assess pore transport. This was examined by studying the performance of the Co/Al_2O_3 catalysts under industrially relevant reaction conditions.

At 483 K and 20 bar ($H_2/CO = 2$), the high metal-specific activities (180 ± 50 $mmol_{CO}\,g_{Co}^{-1}\,h^{-1}$) and turnover frequencies ($4.0 \pm 1.0 \times 10^{-2}$ s^{-1}; Table S1), alongside negligible activities for the water–gas shift reaction (selectivities to $CO_2 < 1\%$), correspond to values expected for catalysts displaying quantitative cobalt reduction (Figure S6) and near-optimal metal dispersion.[12] Regardless of the catalyst porosity, similar hydrocarbon chain-length distributions were obtained, corresponding to industrially relevant chain-growth probabilities (α) of about 0.88 (Figure 3a). In contrast, differences in porosity translated into very remarkable changes in the olefin content of the FT hydrocarbon products. For a given hydrocarbon chain length in the C_3–C_{10} range, the α-olefin-to-paraffin molar ratio obtained with the trimodally porous Co/AO3M catalyst was over one order of magnitude higher than that observed with the mesoporous Co/AO1M catalyst (Figure 3b), resulting in a more than five times higher cumulative α-olefin content (51 vs. 9.5 %; Table S1). The selectivity to C_2–C_4 hydrocarbons was similar for both catalysts at any given CO conversion, for example, 8.4 C-% (on a carbon-atom basis) at $X_{CO} = 30\%$, indicating that α-olefin hydrogenation, rather than chain re-insertion, is primarily responsible for the depletion of these primary reaction products from the ultimate FT hydrocarbon output under the applied reaction conditions. The specific contribution of the macroporosity in Co/AO3M to the preservation of the α-olefin primary products was ascertained by comparison with a series of benchmark Co/Al_2O_3 catalysts synthesized on various mesoporous γ-Al_2O_3 supports (Figure S7 and Table S1). Our analysis revealed that the sub-micrometer effective mesopore transport lengths defined by the dual network of macropores led to a $>50\%$ enhancement in the α-olefin content within the C_{10-} hydrocarbon products owing to their faster evacuation from the catalyst particles, which mitigates secondary hydrogenation reactions, enabling a FT product olefinicity that is out of reach for mesoporous catalyst architectures (Figure S8).

The possibilities offered by the hierarchical porosity to regulate the FT product selectivity, and thus the nature of the intermediate products in the tandem FTS–hydrotreating process, were investigated by the integration of the highly active Co/Al_2O_3 FTS catalysts with a zeolitic Pt/nano-ZSM-5 hydrocracking catalyst (Figures S9 and S10). This catalyst

combination enables the in situ hydrotreating of FT hydrocarbons into target liquid product fractions, that is, in the naphtha (C_5–C_9) and middle-distillates (C_{10}–C_{24}) ranges, which can be cost-effectively transported, even from remote process locations, and further upgraded to reach fuel blending specifications. Owing to its step growth polymerization mechanism, the selectivity of the FTS towards the liquid C_5–C_{24} fraction is inherently limited, for example, to 65 wt% for a chain-growth probability of 0.9, owing to the coproduction of light (tail-gas) hydrocarbons (C_{4-}) and heavy waxes (C_{25+}). Ideally, in situ hydrotreating should convert waxes into liquid fractions, preferably middle distillates, without further contributing to the overall tail-gas production. However, several factors jointly cause methanation, over-cracking, and hydrogenolysis,[15] which generally lead to high selectivities to undesired gas hydrocarbons in the tandem process. These factors include 1) the need for the FTS catalyst to be operated at the higher temperatures required for (hydro)cracking reactions, 2) the perturbation of the bifunctional hydrocracking mechanism by CO inhibition of the (de)hydrogenation functions,[10,16] and 3) the undesired mutual interactions between the FT active species and the acid sites in the hydrocracking catalyst.[9c] Our recent kinetic studies on the conversion of model FT hydrocarbons on a Pt/ZSM-5 hydrocracking catalyst showed that under the syngas atmosphere characteristic of the tandem process, the reaction of α-olefin primary FT products on the hydrocracking catalyst could mitigate this undesired shift of the product distribution towards lighter hydrocarbons by providing a second chain-growth pathway (by short-olefin oligomerization) and curbing over-cracking (by enhanced adsorption competition on the acid sites).[10]

This insight led us to investigate the impact of the FT product regulation, enabled by catalyst porosity design, on the selectivity of the tandem process. Figure 4 summarizes the two different catalyst arrangements that were examined and the corresponding hydrocarbon product distributions. Physical blends of microparticles (500 μm) of the two catalysts operated at a common reaction temperature (523 K) led to similar product distributions regardless of the porosity of the Co/Al_2O_3 FT catalyst. Full wax depletion was achieved, along with selectivities to hydrocarbons in the naphtha range of about 40 wt%. However, high selectivities to C_{4-} hydrocarbons (>30 wt%) were also obtained, in part owing to the excessive cracking of not only waxes but also hydrocarbons in the middle-distillates fraction, whose selectivity did not exceed 25–30 wt%. A very similar product distribution was achieved with a hybrid Co/Al_2O_3-Pt/ZSM-5 (Co/AOZ) composite catalyst in which the spatial proximity between the integrated catalysts is increased from the micrometer to the nanometer regime (Figure S11). These results are well in line with previous studies on the integration of cobalt-based FT catalysts with acidic hydrocracking functionalities at various levels of spatial integration, that is, from catalyst blends[9b,17] to single-particle core–shell arrangements[9a] and zeolite-supported hybrids,[9c,d] and therefore emphasize intrinsic limitations of this tandem process in the selective production of liquid hydrocarbons, particularly middle distillates, without the coproduction of large amounts of gaseous hydrocarbons.

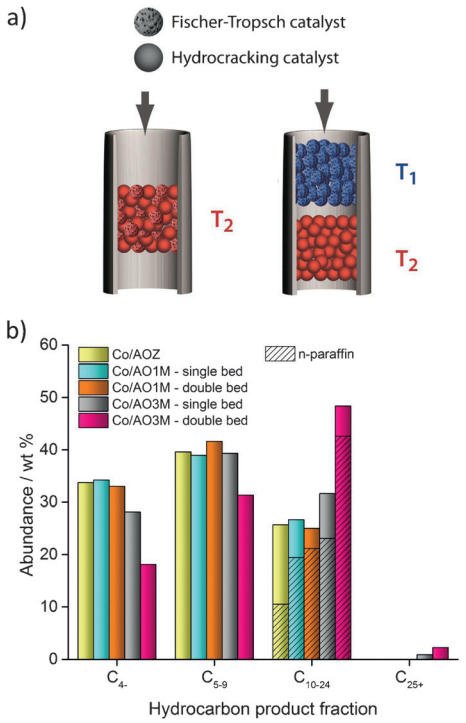

Figure 4. a) Schemes for different spatial and temperature catalyst configurations tested in the tandem Fischer–Tropsch/hydrocracking process. $T_1 = 483$ K, $T_2 = 523$ K. b) Hydrocarbon product distributions obtained by the tandem integration of the unimodally mesoporous Co/AO1M or the trimodally meso/macro/macroporous Co/AO3M Fischer–Tropsch catalysts with a Pt/nano-ZSM-5 hydrocracking catalyst. Data obtained with a hybrid composite catalyst (Co/AOZ, Figure S11) are also shown. Hydrocarbon fractions have been lumped according to the number of carbon atoms in their molecular structure as gases (C_{4-}), naphtha range (C_{5-9}), middle-distillates range (C_{10-24}), and waxes (C_{25+}). For middle distillates, the dashed portion of the bar indicates the contribution from *n*-paraffins. Reaction conditions: $H_2/CO = 2$, $P = 20$ bar, $X_{CO} = 50 \pm 10\%$, and a WHSV of FT hydrocarbons to the hydrocracking catalyst of 2 ± 0.4 g_{CH_2} $g_{HC\ catalyst}^{-1}$ h^{-1}. Duplicates for the test reported in magenta bars showed maximum selectivity differences of ±1 wt% for all reported product hydrocarbon fractions. For the full hydrocarbon distributions, see Figures S12 and S13 and Table S2.

Excessive methanation and hydrogenolysis on the FT catalyst might be mitigated by operating the two catalysts at individually adjusted temperatures, which in turn requires their spatial compartmentalization, for example, in consecutive packed beds or reactor subunits (Figure 4a). Yet, this process configuration led to a product pattern essentially identical to the aforementioned distributions when the conventional mesoporous Co/Al_2O_3 FT catalyst was employed for CO hydrogenation. These results can be rationalized considering that *n*-paraffins are the major FT products processed on the hydrocracking catalyst in all these cases. In the first instance (catalyst blends at 523 K), the higher reaction temperature required for the operation of the hydrotreating catalyst favors hydrogenation chain-termination pathways and thus *n*-paraffin primary products on the FT catalyst, regardless of its structure. In the second instance, this can be attributed to the extensive secondary hydrogenation of the primary FT products within the unimodally mesoporous

Co/AO1M catalyst before they react on the downstream hydrocracking counterpart (Figure 3b). Remarkably, the improved pore transport associated with the trimodal porosity in Co/AO3M enables the spacing of both tandem catalysts (double-bed configuration) and thus an individual temperature adjustment, yet preserving a notably primary nature of the FT hydrocarbon mixture that reacts on the hydrocracking catalyst, largely enriched in C_{10-} α-olefins. Under these conditions, the final product is essentially dewaxed (selectivity to $C_{25+} < 3$ wt%). Most notably, the selectivity to middle distillates is as high as 49 wt%, 88% of which are *n*-paraffins, which are desired as precursors for premium diesel fuels, while the selectivity to tail-gas hydrocarbons remains as low as 18 wt%, that is, a marginal 2% in excess to that in the unprocessed FTS crude. Such a nearly ideal product distribution leads to an unprecedented overall selectivity to liquid hydrocarbon fractions of 80 wt% in a single step, that is, only < 5 wt% lower than what would be achieved if the Fischer–Tropsch waxes were recovered and selectively upgraded into liquids by separate hydrotreating in a conventional two-step process.

In summary, effective sub-micrometer transport distances in a trimodally porous cobalt-based Fischer–Tropsch catalyst enable the channeling of primary FT products onto a tandem hydrocracking catalyst. This permits the operation of the solid catalysts in a spatially and thermally distant fashion, while resembling the case of close site proximity owing to the suppression of secondary reactions of target intermediate products. The catalyst-specific adjustment of the reaction temperature, alongside the mechanistically favorable co-processing of primary α-olefin FT products on the hydrocracking catalyst, enabled simultaneous effective dewaxing with a twofold enhancement in the selectivity to middle-distillates hydrocarbons and a minimum production of undesired gases. These findings suggest means to greatly improve the carbon efficiency of intensified syngas-to-liquid processes. Moreover, we anticipate that the notion of disentangling the effective site proximity from the operating temperature through the regulation of pore mass transport in integrated solid catalysts will be instrumental to realize and optimize other tandem catalytic processes.

Acknowledgements

We are grateful to Sasol and Dr. Patrick Bussian for providing the commercial Al_2O_3 precursor and granulated supports. T. Haak and A. Rocha Vogel, S. Palm, and F. Kohler are thanked for technical assistance with materials synthesis, SEM imaging, and GC analysis, respectively. G.P. acknowledges funding from MPI-KOFO, the European Commission (7th Community Framework Program, PIEF-GA-2013-625167), and the Fonds der Chemische Industrie of Germany.

Conflict of interest

The authors declare no conflict of interest.

Keywords: Fischer–Tropsch catalysis · heterogeneous catalysis · hierarchical porosity · syngas conversion · tandem catalysis

How to cite: *Angew. Chem. Int. Ed.* **2017**, *56*, 11480–11484
Angew. Chem. **2017**, *129*, 11638–11642

[1] F. Nudelman, N. A. J. M. Sommerdijk, *Angew. Chem. Int. Ed.* **2012**, *51*, 6582–6596; *Angew. Chem.* **2012**, *124*, 6686–6700.
[2] Y. S. Hu, P. Adelhelm, B. M. Smarsly, S. Hore, M. Antonietti, J. Maier, *Adv. Funct. Mater.* **2007**, *17*, 1873–1878.
[3] M. Oschatz, L. Borchardt, M. Thommes, K. A. Cychosz, I. Senkovska, N. Klein, R. Frind, M. Leistner, V. Presser, Y. Gogotsi, S. Kaskel, *Angew. Chem. Int. Ed.* **2012**, *51*, 7577–7580; *Angew. Chem.* **2012**, *124*, 7695–7698.
[4] C. M. A. Parlett, K. Wilson, A. F. Lee, *Chem. Soc. Rev.* **2013**, *42*, 3876–3893.
[5] T. Yokoi, T. Tatsumi in *Hierarchically Structured Porous Materials*, Wiley-VCH, Weinheim, **2011**, pp. 481–515.
[6] a) M. J. Climent, A. Corma, S. Iborra, M. J. Sabater, *ACS Catal.* **2014**, *4*, 870–891; b) Y. Yamada, C. K. Tsung, W. Huang, Z. Y. Huo, S. E. Habas, T. Soejima, C. E. Aliaga, G. A. Somorjai, P. D. Yang, *Nat. Chem.* **2011**, *3*, 372–376; c) T. L. Lohr, T. J. Marks, *Nat. Chem.* **2015**, *7*, 477–482.
[7] a) C. You, S. Myung, Y. H. P. Zhang, *Angew. Chem. Int. Ed.* **2012**, *51*, 8787–8790; *Angew. Chem.* **2012**, *124*, 8917–8920; b) I. Wheeldon, S. D. Minteer, S. Banta, S. C. Barton, P. Atanassov, M. Sigman, *Nat. Chem.* **2016**, *8*, 299–309.
[8] a) F. Jiao, J. J. Li, X. L. Pan, J. P. Xiao, H. B. Li, H. Ma, M. M. Wei, Y. Pan, Z. Y. Zhou, M. R. Li, S. Miao, J. Li, Y. F. Zhu, D. Xiao, T. He, J. H. Yang, F. Qi, Q. Fu, X. H. Bao, *Science* **2016**, *351*, 1065–1068; b) K. Cheng, B. Gu, X. L. Liu, J. C. Kang, Q. H. Zhang, Y. Wang, *Angew. Chem. Int. Ed.* **2016**, *55*, 4725–4728; *Angew. Chem.* **2016**, *128*, 4803–4806; c) Q. Zhang, K. Cheng, J. Kang, W. Deng, Y. Wang, *ChemSusChem* **2014**, *7*, 1251–1264; d) S. Sartipi, M. Makkee, F. Kapteijn, J. Gascon, *Catal. Sci. Technol.* **2014**, *4*, 893–907; e) A. Martínez, G. Prieto, *Top. Catal.* **2008**, *52*, 75–90.
[9] a) J. Bao, J. He, Y. Zhang, Y. Yoneyama, N. Tsubaki, *Angew. Chem. Int. Ed.* **2008**, *47*, 353–356; *Angew. Chem.* **2008**, *120*, 359–362; b) A. Freitez, K. Pabst, B. Kraushaar-Czarnetzki, G. Schaub, *Ind. Eng. Chem. Res.* **2011**, *50*, 13732–13741; c) S. Sartipi, K. Parashar, M. J. Valero-Romero, V. P. Santos, B. van der Linden, M. Makkee, F. Kapteijn, J. Gascon, *J. Catal.* **2013**, *305*, 179–190; d) K. Cheng, L. Zhang, J. C. Kang, X. B. Peng, Q. H. Zhang, Y. Wang, *Chem. Eur. J.* **2015**, *21*, 1928–1937.
[10] N. Duyckaerts, I.-T. Trotuş, A.-C. Swertz, F. Schüth, G. Prieto, *ACS Catal.* **2016**, *6*, 4229–4238.
[11] a) E. Iglesia, S. C. Reyes, R. J. Madon, *J. Catal.* **1991**, *129*, 238–256; b) H. Schulz, *Top. Catal.* **2003**, *26*, 73–85.
[12] A. Y. Khodakov, W. Chu, P. Fongarland, *Chem. Rev.* **2007**, *107*, 1692–1744.
[13] P. Munnik, P. E. de Jongh, K. P. de Jong, *Chem. Rev.* **2015**, *115*, 6687–6718.
[14] M. F. M. Post, A. C. Vanthoog, J. K. Minderhoud, S. T. Sie, *AIChE J.* **1989**, *35*, 1107–1114.
[15] X. B. Peng, K. Cheng, J. C. Kang, B. Gu, X. Yu, Q. H. Zhang, Y. Wang, *Angew. Chem. Int. Ed.* **2015**, *54*, 4553–4556; *Angew. Chem.* **2015**, *127*, 4636–4639.
[16] R. Brosius, J. C. Q. Fletcher, *J. Catal.* **2014**, *317*, 318–325.
[17] A. Martinez, J. Rollan, M. A. Arribas, H. S. Cerqueira, A. F. Costa, E. F. S. -Aguiar, *J. Catal.* **2007**, *249*, 162–173.

Manuscript received: June 5, 2017
Accepted manuscript online: July 16, 2017
Version of record online: August 15, 2017

